Nano Research

Open Access

Research Article

A disordered nanostructured surface for ultra-transparent, self-cleaning and durable photovoltaic glass

Yaya Zhou[1], Yaqing Xie[2,3], Ruiyang Chen[2,3], Haixiong Ge[2,3], and Yibing Ma[1] ✉

[1] *Key Laboratory of Functional Materials and Devices for Informatics of Anhui Educational Institutions, Fuyang Normal University, Fuyang 236037, China*
[2] *Department of Materials Science and Engineering, Collaborative Innovation Center of Advanced Microstructures, Jiangsu Key Laboratory of Artificial Functional Materials, College of Engineering and Applied Sciences, Nanjing University, Nanjing 210093, China*
[3] *National Laboratory of Solid State Microstructures, Nanjing 210093, China*

Cite this article: *Nano Research*, **2026**, *19*, 94908912. https://doi.org/10.26599/NR.2026.94908912

ABSTRACT: The persistent decline in photovoltaic efficiency caused by surface soiling represents a major obstacle to the reliable deployment of solar energy systems. While superhydrophobic surface provide a promising route to self-cleaning surfaces, their implementation on photovoltaic glass has been fundamentally constrained by the longstanding trade-off between optical transparency and surface roughness, as well as the reliance on high-temperature fabrication processes. Herein, we provide a feasible approach: optimizing optical, wettability, and mechanical properties simultaneously by designing the height of disordered nanopillar arrays. Unlike prior methods that rely on high-temperature metal dewetting (> 500 °C) or ordered nanostructures requiring expensive lithography, our disordered nanocolumn array (DCA) glass is fabricated via a scalable, substrate-independent route combining block-copolymer phase separation, flexible composite template replication, nanoimprint lithography, plasma etching, and fluorosilane modification. At a nanocolumn height of approximately 150 nm, the surface exhibits a transmittance above 95%, a water contact angle (CA) exceeding 155°, a roll-off angle (RA) as low as 7°. This critical aspect ratio stabilizes the Cassie wetting state while resisting external mechanical stress. This work not only presents a high-performance, durable, and transparent superhydrophobic glass, but also establishes a design paradigm based on geometry engineered disordered nanostructures for multifunctional protective surfaces. It provides the feasible way for more efficient and sustainable solar energy harvesting in real-world environments.

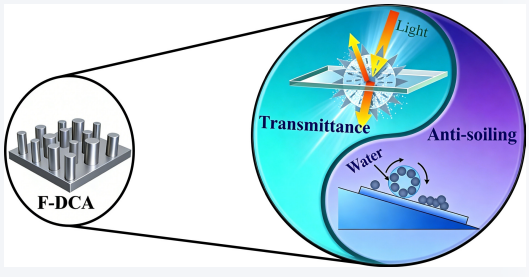

KEYWORDS: photovoltaic cover glass, superhydrophobic, disordered nanocolumn array (DCA), transparency, anti-soiling, durability

1 Introduction

Developing photovoltaic technology that can maintain high photoelectric conversion efficiency over the long term is crucial for the global transition to renewable energy [1–3]. In real outdoor operations, the accumulation of dust, pollen, and other pollutants on the surface of photovoltaic module glass can severely weaken incident light intensity, leading to a sustained decline in the output power of photovoltaic modules [4–7]. Therefore, achieving a self-cleaning capability for the glass cover that is efficient, durable, and does not compromise its core optical functions has become an urgent technical challenge in the photovoltaic field.

Received: March 17, 2026; **Revised:** June 3, 2026
Accepted: June 4, 2026

✉Address correspondence to yibingma@fynu.edu.cn

Currently, strategies for preventing pollution on photovoltaic glass covers can be broadly classified into two categories: passive remediation and active prevention [8–12]. Passive remediation methods, such as manual wiping and mechanical cleaning, can directly remove dirt; however, these methods come with high maintenance costs and also pose a risk of scratching the glass surface [5, 13–15]. In contrast, active prevention strategies based on surface functionalization have the potential to "prevent dirt accumulation before it forms", showing promising prospects. Among these studies, developing surfaces with superhydrophobic or superhydrophilic properties to achieve self-cleaning functions has become a mainstream research direction [16–18]. Superhydrophilic surfaces can form a water film that washes away pollutants, performing well in regions with frequent rainfall [19, 20]. However, their effectiveness significantly decreases in dry, low-rain environments. On the other hand, constructing micro/nano-structured surfaces with low surface energy to achieve

superhydrophobicity results in water droplets forming contact angles greater than 150°, allowing droplets to roll off and carry away contaminants [21–23]. This mechanism is particularly suitable for water-scarce areas and is regarded as a highly promising solution.

Despite extensive research efforts, the practical application of superhydrophobic technology to photovoltaic (PV) glass covers has long been constrained by two core bottlenecks. On the one hand, the microscopic roughness required to achieve superhydrophobicity often induces detrimental light scattering, leading to a loss of the high transparency that glass covers must guarantee [9, 24–26]. On the other hand, most existing fabrication routes require high-temperature annealing (> 500 °C), which is incompatible with polymer substrates and functional layers due to their poor thermal stability [27, 28]. Additionally, most reported superhydrophobic micro-nano structures have limited mechanical strength, making them prone to wear from outdoor dust and raindrop impacts, which in turn causes rapid performance degradation [24]. Previous studies have reported a number of transparent superhydrophobic glass materials fabricated via nanostructure treatment followed by subsequent fluoroalkylsilane modification. For instance, Infante et al. employed metal dewetting combined with reactive ion etching (RIE) to fabricate etched nanostructured glass with low haze, anti-reflection, and superhydrophobic properties [29]. Similarly, follow-up studies further extended this metal dewetting approach to the fabrication of durable transparent superhydrophobic surfaces [30, 31]. Despite these important contributions, they have a common flaw: they rely on high-temperature annealing (> 500 °C) to generate metal nanoparticles as etching masks. This process restricts the practical scalability and industrial applicability of the associated technologies. Furthermore, most of these studies focus exclusively on optimizing the nanostructure etching process, and have not systematically investigated "controlled disorder" as a design principle that can simultaneously balance trade-offs among multiple performance metrics.

In contrast to the high-temperature metal dewetting approach, our study proposes a novel solution: designing a disordered nanostructure array and systematically regulating its geometric parameters to achieve a synergistic optimization of light management, wettability control, and mechanical stability. Moderate structural disorder helps to suppress specific optical interference and diffraction caused by periodic structures, thereby maintaining excellent transparency across a wide spectral range. More importantly, by precisely controlling the height and morphology of the nanostructures, it becomes possible to simultaneously regulate light transmission and superhydrophobicity. This approach transcends the traditional pursuit of "ordered perfect structures", instead viewing "disorder" as a new pathway to address the challenges of multifunctional coupling.

Herein, this work presents the preparation of fluorinated disordered nanocolumn arrays (F-DCA) with varying heights of nanocolumns using nanoimprint lithography (NIL) and inductively coupled plasma reactive ion etching (ICP-RIE) on glass. The systematic investigation focuses on how the height of the nanocolumns (70–380 nm) influences their optical performance, superhydrophobic properties, and mechanical durability. The study reveals an optimized structural height (~ 150 nm) that achieves the best balance among these three performance indicators. Excessively low heights may lead to droplet penetration, while excessively high heights could cause pinning effects on the droplet due to sharp tips formed by over-etching. Nanopillars of a specific height can stabilize the Cassie wetting state. This work not only demonstrates a high-performance transparent superhydrophobic surface suitable for photovoltaic glass but also elucidates a multifunctional synergistic design principle based on disordered nanostructures, providing a feasible approach for developing long-lasting self-cleaning optical devices suitable for harsh outdoor environments.

2 Experimental

2.1 Materials

The Corning Gorilla Glass was procured from Nanjing WanQing Chemical GlassWare & Instrument Co., Ltd. 1H,1H,2H,2H-Perfluorodecyl-trichlorosilane (FDTS) was purchased from Sikang New Material Co., Ltd. Hydrochloric acid, acetone, anhydrous ethanol, toluene, polystyrene (PS), polyphenyl bis-siloxane (PPSQ), polymethyl methacrylate (PMMA) and other reagents were obtained from Aladdin Co., Ltd.

2.2 Disorderly silicon nanohole template preparation

The experimental preparation process is shown in Fig. S1 in the Electronic Supplementary Material (ESM). First, a 3% PMMA solution was spin-coated onto the silicon substrate (3000 rpm, 40 s) to form a uniform film with a thickness of ~ 180 nm. A 25 nm thick SiO_2 intermediate layer was then deposited on the surface using plasma-enhanced chemical vapor deposition (PECVD) to prevent miscibility between the subsequent blended polymer layer and the PMMA layer. A 2% mass fraction of polystyrene/poly(dimethylsiloxane) (PS/PPSQ = 1:1) blended solution was spin-coated onto the PMMA-SiO_2 sample surface at 3000 rpm to form a phase-separated film. The PS phase and the residual PPSQ layer were sequentially removed using ICP-RIE, transferring the pattern to the SiO_2 and PMMA. Next, Chromium was deposited onto the sample surface using an electron beam evaporator (rate: 1 nm/s), achieving the thickness of ~ 20 nm. The chromium-coated sample was immersed in acetone and treated in an ultrasonic cleaning to peel off the PMMA resulting in a disorderly chromium nanonet structure on the surface. Using the chromium layer as a hard mask, ICP-RIE was employed to etch the silicon substrate, obtaining the disorderly nanopore structure. The sample was then placed in a mixed solution of cerium ammonium nitrate, acetic acid, and ultrapure water, followed by ultrasonic treatment to thoroughly remove the residual chromium layer. Finally, the disordered silicon nanopore template was exposed to ozone for 30 min, transferred to a vacuum oven, and functionalized by adding three drops of FDTS at 80 °C under −0.09 MPa for 2 h. This treatment completed the surface hydrophobic modification, yielding a disordered silicon nanopore template suitable for nanoimprinting (Fig. S2 in the ESM).

2.3 F-DCA preparation

Figure 1(a) schematically illustrates the fabrication process of the F-DCA. First, A flexible, transparent polyethylene terephthalate (PET) substrate was spin-coated with a low-surface-energy fluorine UV resist resin (3000 rpm, 40 s). The coated substrate was then aligned with a master disordered silicon nanohole template and nanoimprinted under 0.4 MPa in vacuum. Subsequent UV curing and demolding yielded a complementary polymer-based composite

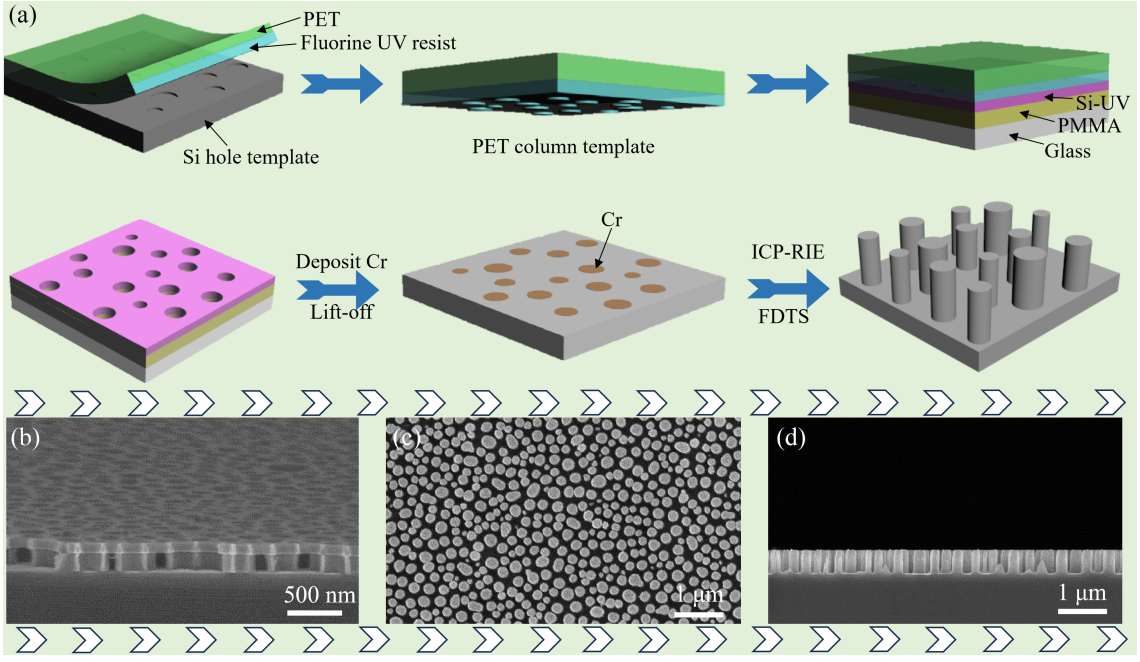

Figure 1 (a) Fabrication processes of the F-DCA. (b)–(d) SEM images of the corresponding disordered nanopore array, Cr dot array, and F-DCA.

template. Subsequent, a 3% solution of PMMA and UV resist was sequentially spin-coated onto a quartz glass substrate. Cover the composite template over the UV resist layer and perform ultraviolet exposure for 60 s in a N_2, thereby forming a disordered nanopore array on the surface of the top UV resist layer (Fig. S3 in the ESM). After demolding, a two-step etching process was performed using an ICP-RIE system. The residual UV resist layer was etched with a mixture of O_2 (20 sccm) and CHF_3 (2 sccm), followed by etching of the underlying PMMA with O_2 (10 sccm). Finally, A ~ 20 nm-thick chromium layer was deposited via electron beam evaporation (PVD). The PMMA layer was removed by ultrasonication in acetone, leaving a disordered chromium (Cr) dot pattern on the quartz surface. Using Cr dot pattern as a hard mask, the quartz glass was etched with a mixture of CHF_3 (30 sccm) and CF_4 (10 sccm). Removal of the Cr produced the disordered nanocolumn array (DCA, Fig. S4 in the ESM) on the quartz substrate. The F-DCA were obtained by exposing the DCA to three drops of FDTS in a vacuum oven at 80 °C and −0.09 MPa for 2 h. Figures 1(b)–1(d) present scanning electron microscopy (SEM) images of the sample at key fabrication stages. As shown in Fig. 1(b), the two-step etching process completely removed the residual UV resist and the underlying PMMA layer, yielding polymer nanopores. Figure 1(c) demonstrates the resulting disordered Cr dot array, which exhibits excellent consistency with the geometric parameters of the original silicon nanohole template, thereby attesting to the high fidelity and reliability of our pattern transfer strategy. The structurally intact disordered nanocolumn array, showcased in Fig. 1(d), confirms the successful implementation of the entire fabrication protocol.

2.4 Fluorinated ordered nanocolumn arrays preparation

Using the same fabrication process as that of F-DCA, an ordered nanocolumn array (diameter of 200 nm, periodicity of 400 nm, and height of 300 nm, Fig. S5 in the ESM) was fabricated on quartz glass as a control sample, with the only difference being the use of an ordered silicon template.

2.5 Characterizations

The surface morphology of the samples was characterized using a scanning electron microscope (GeminiSEM, ZEISS) operated at an accelerating voltage of 20 kV. To evaluate the transmittance and reflectance of light, a UV-3600 ultraviolet–visible spectrophotometer was used. Static contact angle and roll-off angle measurements were conducted using a fixed-drop analyzer (DSA100, Krüss, Germany). Measurements were taken at three different locations on each surface, and the average value was calculated. Unless otherwise specified, the droplet volume used for both contact angle and roll-off angle measurements was 5 μL, with three independent measurements taken on different regions of the sample surface. Relevant optical images were recorded using a camera (SONY NEX-7) with a macro lens.

3 Results and discussion

3.1 Characterization of structure and optical properties

As shown in Figs. 2(a)–2(d), we fabricated a series of disordered nanocolumn arrays (DCA) with heights of 70, 150, 250, and 380 nm by controlling the quartz etching time. Subsequently, all samples were surface-treated with FDTS to reduce their surface energy. The resulting samples were labeled according to their heights as F-DCA-70, F-DCA-150, F-DCA-250, and F-DCA-380. When the nanocolumn heights were 70 and 150 nm, there was no noticeable difference between the top and bottom diameters. However, as the etching time increased, the top diameter became slightly smaller than the bottom diameter when the nanocolumn height reached 250 nm. This was due to the lateral etching of the nanocolumn sidewalls by the reactive plasma during the etching process, with the top experiencing more etching than the bottom. When the nanocolumn height was further increased to 380 nm, the lateral etching effect became more pronounced, not only causing the top diameter to be significantly smaller than the bottom but also enlarging the gap between adjacent nanocolumns at the top.

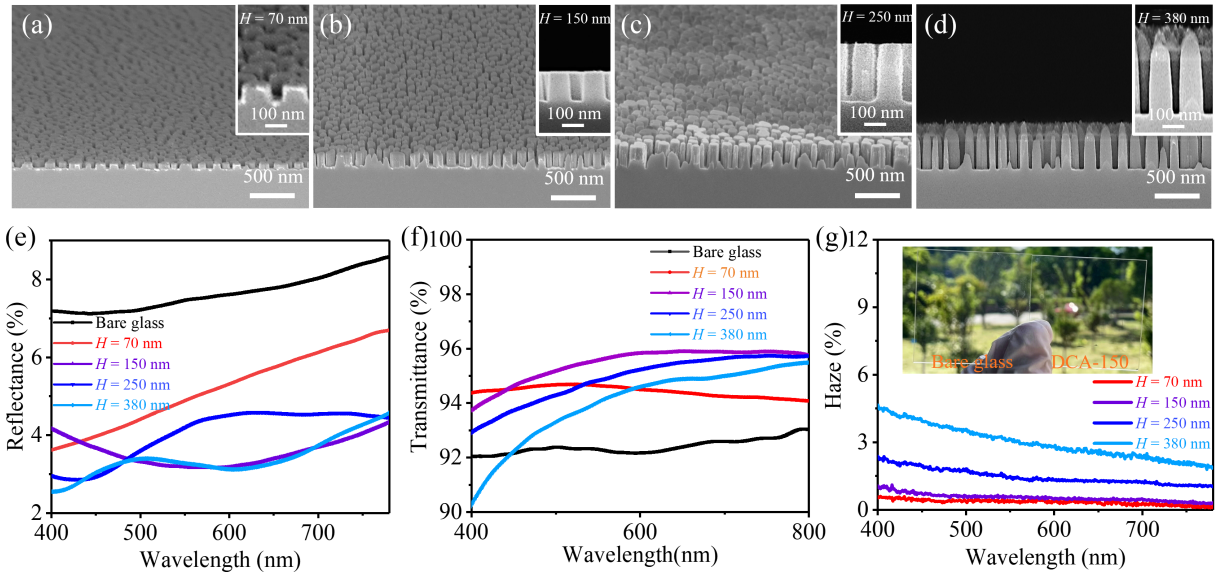

Figure 2 (a)–(d) The heights of the disordered nanocolumns were respectively labeled as F-DCA-70, F-DCA-150, F-DCA-250, and F-DCA-380. (e) and (f) Reflectance and transmittance of F-DCA-(70, 150, 250 and 380) and bare glass. (g) The haze of different sample and tree captured through F-DCA-150.

Transparent glass is commonly used as a protective layer in devices such as displays, touchscreens, and solar cells, and its optical properties directly influence the overall performance of the devices. Typically, the construction of micro/nanostructures on the glass surface significantly affects its light transmission properties. To investigate this, we characterized the optical performance of bare glass and samples with different heights of disordered nanocolumns using a UV-3600 ultraviolet-visible spectrophotometer. As shown in Fig. 2(e), compared to the blank substrate and ordered nanocolumn array (Fig. S6 in the ESM), the samples with the disordered nanocolumn structures exhibited a significant reduction in reflectance, indicating that the structure effectively suppressed interface reflection. Additionally, these samples demonstrated higher transmittance (Fig. 2(f)). The images and text displayed in Fig. S7 in the ESM, captured through DCA glass, show superior clarity compared to bare glass and ordered nanocolumn array (noticeable rainbow effect, Fig. S8 in the ESM), further confirming that introducing disordered nanocolumn structures on quartz glass can achieve both antireflection and antireflection enhancement. The reason behind this lies in the fact that the disordered arrangement of the nanocolumns enables incoherent scattering of incident light at the interface. This mechanism distributes the energy uniformly across all angles, rather than concentrating it in a specific direction. As a result, the disordered nanocolumn array maintains high surface roughness while maximizing optical transparency (Fig. S9 in the ESM).

To assess the potential application of the disordered nanocolumn array in imaging and display fields, we performed haze characterization of the prepared samples. Figure 2(g) shows the haze data calculated according to Eq. (1) [32]

$$h_\lambda = \frac{S_{d,\lambda}}{S_{t,\lambda}} - \frac{W_{d,\lambda}}{W_{t,\lambda}} \quad (1)$$

where $S_{d,\lambda}$ and $S_{t,\lambda}$ represent the scattering transmittance and total transmittance of the sample, respectively, while $W_{d,\lambda}$ and $W_{t,\lambda}$ refer to the scattering transmittance and total transmittance measured when the sample is removed from the optical path of the spectrometer.

It can be seen that within the short-wavelength range, the haze of all samples is higher than that in the long-wavelength range (Fig. 2(g)), and the haze increases with the height of the nanocolumns. The samples with heights of 70 and 150 nm exhibited relatively low haze, remaining below 1% in the 400–780 nm wavelength range, indicating better transparency for these two samples. To visually verify these results, we observed outdoor scenes through bare glass and glass with a 150 nm disordered nanocolumn array on the surface. The glass with the nanocolumn structure had minimal impact on visual observation, and the outdoor scenes were still clearly visible, further demonstrating that the nanocolumn array at this height can maintain good imaging quality while achieving antireflection.

3.2 Superhydrophobic and anti-dust properties

In the following, the surface liquid-repellent performance of quartz samples with F-DCA of different heights was characterized. The results showed that the contact angle variation of water and oleic acid on the surface followed similar patterns (Fig. 3(a)). When the nanocolumn height was 70 nm, the contact angle (CA) was the smallest (water CA = 141.7° and oleic acid CA = 130.5°), and water droplets could not roll off (rolling angle (RA) >90°). This unique wetting behavior does not stem from a simple Wenzel state; instead, it is a transition wetting state induced by the insufficient height of the nanostructures. Under droplet weight or minor disturbances, the liquid-air interface can easily sag and make substantial contact with the substrate between the nanocolumns [33], leading to a high-adhesion, Wenzel-like state (Fig. S10 in the ESM). This explains the observed contact angle reduction and the complete pinning of droplets. As the height increased to 150 nm, the water and oleic acid CA significantly increased (water CA = 155.3° and oleic acid CA = 141.6°), and the RA of the water droplets decreased to 7°, with the sample exhibiting excellent liquid-repellent and self-cleaning properties. This improvement was due to the sufficient height of the nanocolumns to prevent droplets from touching the bottom, thus enhancing the liquid-repellent performance (Fig. S11 in the ESM). For the ordered nanocolumn array, the surface CA is 152° (Fig. S12 in the ESM), which is comparable to that of F-DCA-

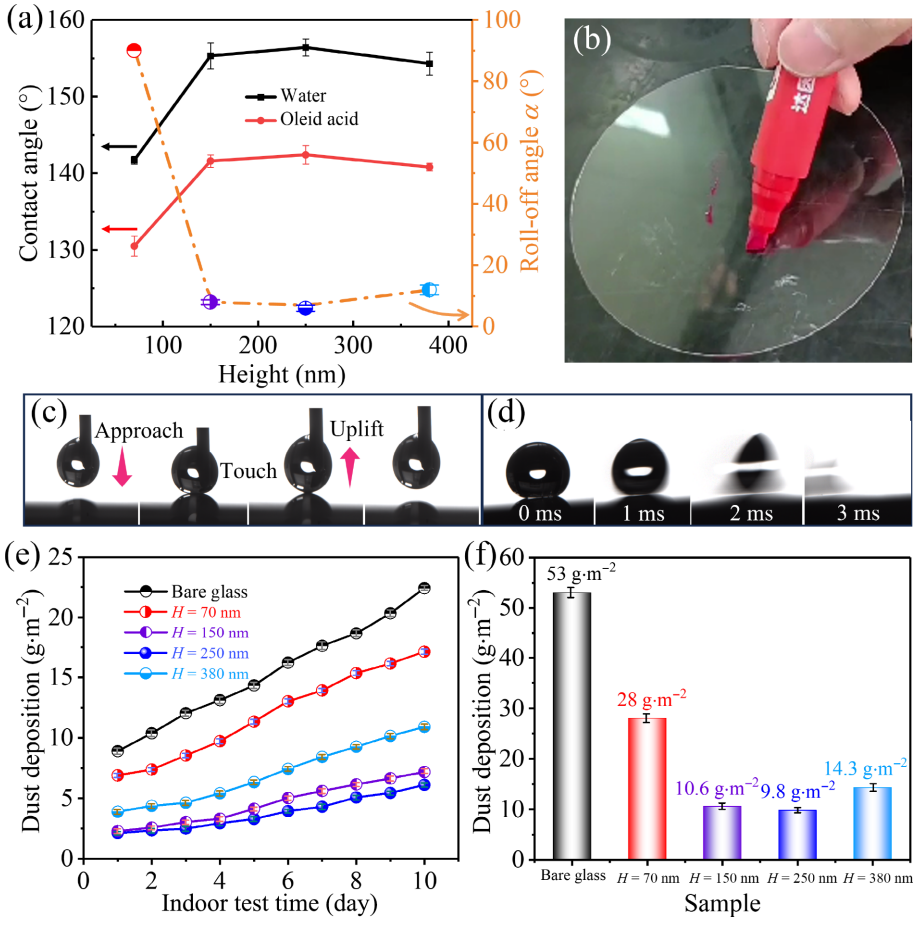

Figure 3 (a) The CA and RA of F-DCA-(70, 150, 250 and 380). (b) The picture after the marker pen was drawn on the surface of F-DCA-150. (c) The process of a water droplet being in contact with and lifted from the F-DCA-150. (d) The water droplet rolls off the sample surface at an angle of only 15°. (e) Dust deposition amount after 10 days indoor test. (f) Dust deposition amount after 180 days outdoor exposure test.

150. When the height was further increased to 250 nm (water CA of 156.4°, an oleic acid CA of 142.4°, and a water RA of 6°), the liquid-repellent properties and rolling angle were comparable to those of the 150 nm sample (water CA of 155.3°, an oleic acid CA of 141.6°, and a water RA of 7°). However, when the height reached 380 nm, the contact angle began to decrease, and the rolling angle increased. This could be attributed to over-etching, which caused the nanocolumn tips to become sharper, reducing the support for the droplets and thereby triggering the pinning effect (Fig. S13 in the ESM). Similar geometric effects on wetting transitions have been extensively discussed in studies [34, 35].

We selected F-DCA-150 quartz glass, which exhibits both excellent optical properties and high liquid-repellent performance, to further assess its applicability and stability in real-world scenarios. As shown in Fig. 3(b), after a marker pen was drawn across the F-DCA-150 surface, the ink aggregated and contracted, while on the bare glass surface, it spread uniformly (Fig. S14 in the ESM), indicating the excellent liquid-repellent properties of F-DCA-150. Further dynamic experiments were conducted to verify its hydrophobicity: when an 8 μL water droplet was moved and lifted by a syringe needle on the surface of the sample, no significant deformation of the droplet occurred (Fig. 3(c)), suggesting that the needle-water interface force ($F_{\text{needle-water}}$) was sufficient to overcome the gravity of droplet (G_{water}) and adhesion to the surface ($F_{\text{surface-water}}$, Fig. S15 in the ESM). Additionally, a 10 μL water droplet rapidly rolls off the sample surface at a tilt angle of only 15° within 3 ms, leaving no residue, indicating extremely low water adhesion and outstanding dynamic superhydrophobic performance (Fig. 3(d)).

To evaluate the dust resistance performance of the fabricated surfaces, both outdoor static dust resistance testing and indoor simulated dust resistance experiments were conducted. In the outdoor test, the samples were placed in Petri dishes and fixed at a 20° tilt angle on a balcony. The dust resistance was assessed by measuring the weight change after different exposure durations. The indoor test employed a 200-mesh-sieved outdoor soil dust at a concentration of 500 g·m^{-3} in a dedicated chamber with a 20° tilt angle, and three samples were tested for each condition to enable statistical evaluation [36]. As shown in Fig. 3(e), after 10 days of indoor testing, the dust deposition on the F-DCA-150 and F-DCA-250 surfaces was 7.3 and 6.1 g·m^{-2}, respectively, significantly lower than that on the bare glass, F-DCA-70, and F-DCA-380 samples. After 180 days of outdoor exposure, the dust accumulation on the F-DCA-150 and F-DCA-250 surfaces was 10.6 and 9.8 g·m^{-2}, respectively, still much lower than on the bare glass (53 g·m^{-2}), F-DCA-70 (28 g·m^{-2}), and F-DCA-380 (14.3 g·m^{-2}), clearly demonstrating the excellent dust resistance of these two surfaces (Fig. 3(f)). The increased dust accumulation on the F-DCA-380 surface is due to two factors: (1) larger inter-column gaps that allow dust particles to become trapped; and (2) an excessive aspect ratio that may create capillary effects, drawing fine dust particles into the gaps. To further explore the dust resistance mechanism, the surface morphology after 180 days of outdoor exposure was analyzed. As

shown in Fig. S16 in the ESM, the densely arranged nanocolumn structures reduce the likelihood of dust particles entering the gaps between the structures, causing dust to primarily accumulate at the tops of the nanocolumns. This arrangement decreases the actual contact area between the dust and the glass substrate, thereby reducing adhesion strength. Consequently, under the influence of external forces such as gravity or wind, dust particles are more easily detached from the surface, exhibiting significant dust resistance performance. Notably, while all F-DCA samples exhibit hydrophobic properties, their anti-dust performance varies significantly with geometry (Table S1 in the ESM). This indicates that the structural geometry plays a more critical role in determining dust removal efficiency under dry conditions.

3.3 Mechanical stability

Superhydrophobic self-cleaning surfaces often face various mechanical challenges in practical applications [37]. Therefore, it is essential to evaluate their mechanical stability and wear resistance. To evaluate the mechanical robustness of DCA-150, a sandpaper abrasion test was first conducted (Fig. 4(a)). The sample (5 cm × 5 cm) was placed on sandpaper (grit No. 800) and subjected to movement under a weight of 500 g. Each reciprocating motion covering a total distance of 2.5 m on the sandpaper is defined as one friction cycle. The results showed that after 20 cycles (total wear distance of 50 m), both the contact angle and rolling angle on the DCA-150 surface did not exhibit significant changes, maintaining a stable superhydrophobic state (Fig. 4(b)). Further, a sand impact test was conducted on DCA-150 according to the ISO/TS 10,689:2023 standard [38] (Fig. S17 in the ESM). After 300 sand impact cycles, the water CA on its surface remained stable at approximately 161.7° (Fig. 4(d)), with no significant decrease, further confirming its excellent impact resistance. The results of both the sandpaper abrasion and sand impact tests demonstrate that DCA-150 possesses outstanding mechanical robustness. To investigate the mechanism behind the exceptional durability of DCA-150, SEM characterization was performed on the samples after abrasion and sand impact treatments (Fig. S18 in the ESM). The results showed that the disordered nanocolumn structure on its surface remained intact after testing. This is primarily attributed to the fact that (i) the nanocolumns are directly etched into the quartz substrate via ICP-RIE, forming a monolithic structure that avoids the weak interfacial adhesion common in coated systems; (ii) quartz glass itself has high hardness; (iii) the disordered arrangement helps distribute external stress across multiple columns rather than concentrating it on a few; (iv) the FDTS forms covalent bonds with hydroxyl groups on the nanocolumn surfaces, enhancing chemical stability. To further evaluate the practical self-cleaning performance, the DCA-150 surface was contaminated with adhesive carbon powder after gravel impact testing. When tilted at 20°, rolling water droplets completely removed the dust particles without leaving any residue (Fig. S19 in the ESM), confirming that the surface retains its self-cleaning functionality even after undergoing mechanical abrasion, further demonstrates the potential of DCA-150 for practical applications.

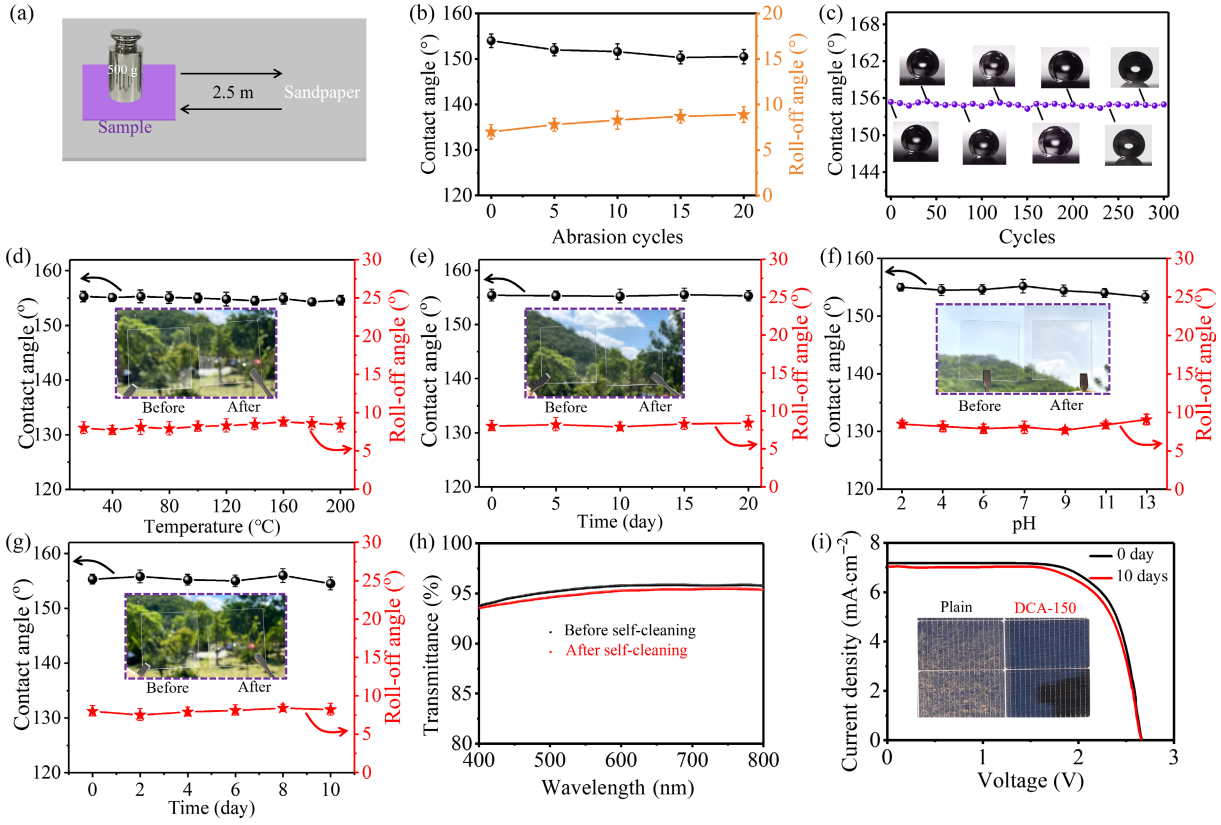

Figure 4 (a) Schematic of sandpaper abrasion test (one cycle). (b) Changes in CA and RA after mechanical abrasion cycles of DCA-150. (c) Changes in CA after impact test cycles of DCA-150. (d) The variation of CA and RA as a function of the temperature. (e) The variation of CA and RA as a function of the irradiation UV time. (f) The variation of CA and RA as a function of the pH of solution for 10 days. (g) The variation of CA and RA as a function of the humidity. (h) Transmittance of DCA-150 samples after self-cleaning test. (i) The comparison of *I*–*V* curves of the solar cells with DCA-150. Inserted: photographs of the assembled solar cell covered with transparent superhydrophobic glass.

3.4 Environmental and chemical durability

To further evaluate the practical durability of the F-DCA-150 samples under complex environmental conditions, a systematic assessment was conducted, encompassing thermal stability, UV stability, chemical stability, and humidity resistance. To evaluate the thermal stability of F-DCA-150, the samples were placed at different temperatures ranging from 20 to 200 °C, maintaining each temperature for 2 h. As shown in Fig. 4(d), the surface of F-DCA-150 maintained its CA, RA, and transparency (inset in Fig. 4(d)) even at the high temperature of 200 °C, demonstrating excellent thermal stability. This is primarily attributed to the outstanding thermal stability of the quartz substrate, and the covalent bonds formed between FDTS and hydroxyl groups on the nanopillar surfaces, which provide exceptional heat resistance. In order to assess the UV stability of F-DCA-150, sample were subjected to accelerated UV irradiation for 20 days, while the CA and RA were measured at 5 days intervals, as depicted in Fig. 4(e). The results revealed that the CA and RA remained unchanged. This stability is attributed to the chemical inertness of the perfluorinated groups and the robustness of the integrated quartz nanopillar array. The inset in Fig. 4(e) visually confirms that the optical clarity of the samples was unaffected before and after UV exposure. Additionally, F-DCA-150 was immersed in deionized water and solutions with different pH values adjusted by tuning dilute hydrochloric acid and sodium hydroxide solutions, for 10 days. After immersion, the sample were rinsed with deionized water and dried, followed by testing their surface wetting behavior. As showed in Fig. 4(f), the results showed no significant changes in CA and RA after 10 days of immersion in deionized water and different pH environments, indicating that F-DCA-150 possesses high chemical stability. Finally, to assess its humidity resistance, we conducted a continuous 10 days humidity test in a salt spray chamber, measuring the CA and RA every 2 days. As shown in Fig. 4(g), the CA and RA remained unchanged throughout the testing period. This can be attributed to the high CA and low RA of the surface, which enabled condensed water droplets to be effectively removed, thereby maintaining stable wetting performance.

To appropriately position the performance of F-DCA-150, we conducted a systematic comparison with representative transparent superhydrophobic surfaces reported in recent literature (Table S2 in the ESM). While certain individual metrics may be surpassed by specific designs, such as Nomeir et al. reporting a higher CA of 173.6°, their transparency significantly decreased to 82.1%, and no dust resistance evaluation was conducted [39]. Furthermore, Infante et al. demonstrated excellent optical performance, with a reflectance below 0.4% and haze below 0.9%, but did not assess dust resistance [29]. In contrast, F-DCA-150 coordinates high transparency (> 95%), low haze (< 1%), superhydrophobicity (CA > 155°, RA < 7°), dust resistance (10.6 $g \cdot m^{-2}$), and durability (mechanical, environmental and chemical) within a single nanostructured surface. This comprehensive synergy of multiple performances is uncommon in existing reports. Additionally, the phase-separation-based template method eliminates the need for high-temperature processing, enhancing substrate versatility and compatibility with low-cost, large-area manufacturing. This further distinguishes this method from previous techniques that rely on thermal dewetting or laser-based patterning [30, 40–42]. Clearly, F-DCA-150 exhibits outstanding performance across multiple dimensions, demonstrating significant potential for practical applications.

3.5 The energy-conversion performance of self-cleaning solar cells

To evaluate the functional durability of the DCA-150 surface under practical operating conditions, its optical transmittance was characterized before and after the self-cleaning process. As shown in Fig. 4(e), the transmittance after cleaning remained stable and was consistently higher than that of the bare glass substrate. This result confirms that the surface maintains its anti-fouling functionality without compromising the light-harvesting capability essential for photovoltaic applications. To further validate its application value, DCA-150 glass was integrated with commercial solar cells to construct a functional photovoltaic device (as depicted in the inset of Fig. 4(f)). Notably, this device exhibited sustained high photoelectric conversion efficiency, attributed to the synergistic optical effects of the disordered nanocolumn array. The disordered nanocolumn structure on its surface facilitated multiple reflections and refractions of the incident light at the air–glass interface [43, 44], effectively suppressing surface reflection losses and enhancing light coupling into the active layer (Fig. 4(f)). These results indicate that DCA-150 glass serves a dual purpose as both a protective barrier and an optical enhancement layer, providing a synergistic pathway for practical photovoltaic systems.

4 Conclusions

In summary, this study has coordinated the contradiction between the superhydrophobicity and optical transparency of photovoltaic glass by manipulating the surface nanostructures, providing a feasible technical solution for the practical application of photovoltaic protective glass. The F-DCA developed herein realizes the synergistic optimization of conflicting macroscopic properties: it maintains high optical transmittance (> 95%) while achieving superhydrophobicity (CA > 155°, RA < 7°), attributed to the incoherent scattering effect of the disordered nanostructure that mitigates light loss caused by surface roughness. Notably, the F-DCA exhibits exceptional durability, maintaining its structure and performance under sandpaper abrasion (50 m, 500 g), sand impact (300 cycles), thermal treatment (20–200 °C), UV irradiation (20 days), high humidity (10 days), and immersion in pH 2–13 solutions (10 days). This durability, coupled with superior anti-soiling performance (10.6 $g \cdot m^{-2}$ dust accumulation after 180 days of outdoor exposure), addresses the core requirements for long-term outdoor service of photovoltaic modules. However, the current work lacks relevant assessments of real long-term outdoor experiments on solar cell modules covered with unordered nanocolumn glass, which will be a focus of future research. Furthermore, the approach that combines scalable nanoimprint lithography (NIL) with established etching processes demonstrates significant application potential.

Electronic Supplementary Material: Supplementary material (structure characterization, wettability characterization, spectra, self-cleaning, and results) is available in the online version of this article at https://doi.org/10.26599/NR.2026.94908912.

Data availability

All data needed to support the conclusions in the paper are presented in the manuscript and the Electronic Supplementary Material. Additional data related to this paper may be requested from the corresponding author upon request.

Acknowledgements

This work was joint support by the National Natural Science Foundation of China (Nos. 12504125 and 51721001), the Key Research and Development Program of Jiangsu Provincial Department of Science and Technology of China (No. BE2019002), Scientific Research Project of Fuyang Normal University (Nos. 2024KYQD0061 and 2024KYQD0063), Open Project Program of the Anhui Province Key Laboratory of Information Materials and Devices (Nos. FMDI202504 and FMDI202506), and Excellent Research and Innovation Team of Functional Materials and Devices for Informatics of Anhui Higher Education Institute (No. 2024AH010024).

Declaration of competing interest

All the contributing authors report no conflict of interests in this work.

Author contribution statement

Y. Y. Z.: Conceptualization, methodology, data curation, writing – original draft, project administration, funding acquisition. Y. Q. X.: Methodology, data curation. R. Y. C.: Methodology, formal analysis. H. X. G.: Project administration, funding acquisition. Y. B. M.: Methodology, project administration, writing – review & editing.

Use of AI statement

None.

References

[1] Verduci, R.; Romano, V.; Brunetti, G.; Yaghoobi Nia, N.; Di Carlo, A.; D'Angelo, G.; Ciminelli, C. Solar energy in space applications: Review and technology perspectives. *Adv. Energy Mater.* **2022**, *12*, 2200125.

[2] Khan, S. Y.; Rauf, S.; Liu, S. L.; Chen, W.; Shen, Y. L.; Kumar, M. Revolutionizing the solar photovoltaic efficiency: A comprehensive review on the cutting-edge thermal management methods for advanced and conventional solar photovoltaics. *Energy Environ. Sci.* **2025**, *18*, 1130–1175.

[3] Yao, Q. C.; Song, H. X.; Zhang, M. S.; Yu, W. Z.; Shao, J. Q.; Liang, H. W.; Dong, X. X. Recent advances in semi-transparent perovskite solar cells: Fabrication, structural engineering, applications, and future challenges. *J. Mater. Chem. C* **2025**, *13*, 22059–22103.

[4] Xiao, X. C.; Chalh, M.; Loh, Z. R.; Mbina, E.; Xu, T.; Hiorns, R. C.; Li, Y. J.; Das, M.; N'konou, K.; Ng, L. W. T. Strategies to achieve efficiencies of over 19% for organic solar cells. *Cell Rep. Phys. Sci.* **2025**, *6*, 102390.

[5] Alkharusi, T.; Russo, G.; Oyeniran, A.; Pandey, C.; Buonomano, A.; Palombo, A.; Markides, C. N. Quantifying the influence of soiling on PV module energy production based on a coupled opto-thermal-electrical model: An international assessment in different climatic conditions. *Renew. Energy* **2026**, *256*, 124119.

[6] Yoon, J.; Hou, Y. C.; Knoepfel, A. M.; Yang, D.; Ye, T.; Zheng, L. Y.; Yennawar, N.; Sanghadasa, M.; Priya, S.; Wang, K. Bio-inspired strategies for next-generation perovskite solar mobile power sources. *Chem. Soc. Rev.* **2021**, *50*, 12915–12984.

[7] Olorunfemi, B. O.; Ogbolumani, O. A.; Nwulu, N. Solar panels dirt monitoring and cleaning for performance improvement: A systematic review on smart systems. *Sustainability* **2022**, *14*, 10920.

[8] Wang, D. H.; Sun, Q. Q.; Hokkanen, M. J.; Zhang, C. L.; Lin, F. Y.; Liu, Q.; Zhu, S. P.; Zhou, T. F.; Chang, Q.; He, B. et al. Design of robust superhydrophobic surfaces. *Nature* **2020**, *582*, 55–59.

[9] Oh, S.; Cho, J. W.; Lee, J.; Han, J.; Kim, S. K.; Nam, Y. A scalable haze-free antireflective hierarchical surface with self-cleaning capability. *Adv. Sci.* **2022**, *9*, 2202781.

[10] Zhu, C. X.; Yu, X. Y.; Lv, J.; Zhang, J.; Yang, J. T.; Hao, N.; Feng, J. Antisoiling performance of lotus leaf and other leaves after prolonged outdoor exposure. *ACS Appl. Mater. Interfaces* **2020**, *12*, 53394–53402.

[11] Wang, Y. C.; He, J. H. Recent progress in outermost surface engineering for solar panels. *Nanoscale* **2025**, *17*, 16071–16099.

[12] Xu, K.; Chen, C. S.; Yuan, S. Biomimetic porous ceramics with stomata-inspired architecture for high-efficiency and durable solar steam generation. *Chem. Eng. J.* **2025**, *522*, 167471.

[13] Adak, D.; Bhattacharyya, R.; Barshilia, H. C. A state-of-the-art review on the multifunctional self-cleaning nanostructured coatings for PV panels, CSP mirrors and related solar devices. *Renew. Sustain. Energy Rev.* **2022**, *159*, 112145.

[14] Sepúlveda-Oviedo, E. H. Optimizing PV maintenance: Methods, cleaning frequency, and a selection protocol. *Energy Rep.* **2025**, *14*, 1578–1605.

[15] Ahmadullah, A. B.; Bakhtyal, I. A.; Irshad, A. S.; Doost, Z. H.; Wali, N.; Karimi, B. A. Comparative assessment of optimal cleaning schedules for various PV cleaning techniques. *Renew. Energy* **2026**, *256*, 124182.

[16] Chen, Z.; Jiang, Z. Y.; Lu, S.; Song, Z. H.; Zhang, G. J.; Han, F. L. Sustainable preparation of a superhydrophobic and low-reflective polymer film with hierarchical microstructure for solar cells. *ACS Appl. Mater. Interfaces* **2025**, *17*, 65086–65101.

[17] Liu, Z. X.; Si, Y. F.; Yu, C. L.; Jiang, L.; Dong, Z. C. Bioinspired superwetting oil-water separation strategy: Toward the era of openness. *Chem. Soc. Rev.* **2024**, *53*, 10012–10043.

[18] Meng, L. J.; Awashra, M.; Hamed, S.; Gnatyuk, D.; Vähänissi, V.; Jokinen, V.; Savin, H.; Liu, X. L. Femtosecond-laser-surface-nanostructured glass for building-integrated photovoltaics. *Mater. Des.* **2025**, *252*, 113745.

[19] Liu, L.; Gao, X. Y.; Zheng, S. S.; Yao, X.; Ju, J.; Jiang, L. Recent progress on liquid superspreading and its applications. *Adv. Mater.* **2025**, *37*, 2501734.

[20] Xie, Y.; Xiong, W.; Kareem, S.; Qiu, C. X.; Hu, Y. F.; Parkin, I. P.; Wang, S. W.; Wang, H. Y.; Chen, J. W.; Li, L. et al. Robust superamphiphobic coatings with gradient and hierarchical architecture and excellent anti-flashover performances. *Nano Res.* **2022**, *15*, 7565–7576.

[21] Chen, F. Z.; Wang, Y. Q.; Tian, Y. L.; Zhang, D. W.; Song, J. L.; Crick, C. R.; Carmalt, C. J.; Parkin, I. P.; Lu, Y. Robust and durable liquid-repellent surfaces. *Chem. Soc. Rev.* **2022**, *51*, 8476–8583.

[22] Tang, Z. Q.; Tian, T. F.; Molino, P. J.; Skvortsov, A.; Ruan, D.; Ding, J.; Li, Y. L. Recent advances in superhydrophobic materials development for maritime applications. *Adv. Sci.* **2024**, *11*, 2308152.

[23] Liu, J.; Wang, X. J.; Zheng, N.; Yao, P.; Zhang, Y. Y.; Xia, F.; Zhang, H. H.; Wang, P.; Zhang, C. M.; Min, X. et al. Biomimetic fluorinated polysiloxane/polyurea-silica coating with rapid self-healing and anti-icing performances. *Nano Res.* **2025**, *18*, 94907514.

[24] Wang, Y. X.; Sun, R.; Zhao, W.; Lu, X. B.; Xiao, W. Q.; Meng, F. D.; Zhan, X. L.; Lu, J. G.; Gao, F.; Zhang, Q. H. Transparent, anti-fouling and mechanically stable coating with hybrid architecture inspired by corn bracts-coating strategy. *Adv. Funct. Mater.* **2025**, *35*, 2418795.

[25] Li, H.; Tu, S. H.; Tu, H. Y.; Chen, M.; Zhou, S. X.; Wu, L. M. Construction of transparent, robust and haze-selectable superhydrophobic coatings with honeycomb structure. *Chem. Eng. J.* **2024**, *483*, 149319.

[26] Liu, Y. J.; Guo, Y. J.; Zhang, X. Q.; Gao, G. Q.; Shi, C. Q.; Huang, G. Z.; Li, P. L.; Kang, Q.; Huang, X. Y.; Wu, G. N. Self-cleaning of superhydrophobic nanostructured surfaces at low humidity enhanced by vertical electric field. *Nano Res.* **2022**, *15*, 4732–4738.

[27] Ben Dkhil, S.; Pfannmöller, M.; Schröder, R. R.; Alkarsifi, R.; Gaceur, M.; Köntges, W.; Heidari, H.; Bals, S.; Margeat, O.; Ackermann, J. et al. Interplay of interfacial layers and blend composition to reduce thermal degradation of polymer solar cells at high temperature. *ACS Appl. Mater. Interfaces* **2018**, *10*, 3874–3884.

[28] Jeon, Y. S.; Park, N. G. Nickel oxide thin films formed from the pH-adjusted solutions for inverted perovskite solar cells. *ACS Energy Lett.* **2025**, *10*, 1266–1274.

[29] Infante, D.; Koch, K. W.; Mazumder, P.; Tian, L. L.; Carrilero, A.; Tulli, D.; Baker, D.; Pruneri, V. Durable, superhydrophobic, antireflection, and low haze glass surfaces using scalable metal dewetting nanostructuring. *Nano Res.* **2013**, *6*, 429–440.

[30] Wang, W.; Mao, Z. P.; Liu, P.; Deng, W. L.; Gu, W. C.; Yu, X. Q.; Zhang, Y. F. Compact nanopillar array with enhanced anti-accumulation of multiphase matter on transparent superhydrophobic glass. *J. Mater. Chem. A* **2023**, *11*, 18679–18688.

[31] Wu, X. H.; Zhou, X.; Xu, K. H.; Tan, G. H.; Mai, J. X.; Ye, Z. L.; Lai, Y. K.; Huang, J. Y.; Hu, J.; Chen, Z. Nano-grid enhanced hierarchical structure construction for a durable, bendable, anti-condensation and passive-active anti-/deicing surface. *J. Mater. Chem. A* **2025**, *13*, 32886–32898.

[32] Wang, W.; Gao, J. H.; Hu, H. B.; Jiang, Y. X.; Wu, H. C.; Li, X. Y.; Li, X. H.; Liang, L. Y.; Zhang, H. L.; Cao, H. T. Air nanocolumn-SiO_2 composite film with adjustable anisotropic refractive index. *Mater. Today Phys.* **2022**, *26*, 100722.

[33] Zhou, M.; Lin, Y. J.; Geng, Z. L.; Zhang, F. Y.; Zhou, L. M.; Shen, Y.; Zhang, L. J.; Ding, W.; Bonaccurso, E.; Chen, L. Q. et al. Dual pathways of air cavity evolution during droplet impact on superhydrophobic nanoporous surfaces. *Phys. Rev. Lett.* **2026**, *136*, 114001.

[34] Huang, G.; Yang, Z.; Zheng, G. H. Pinning effect and energy barrier of sharp edges of water droplet advancing wetting on pore-featured planes. *Colloids Surf. A: Physicochem. Eng. Asp.* **2025**, *725*, 137562.

[35] Luo, Z.; Mehraeen, S. Molecular view of the distortion and pinning force of a receding contact line: Impact of the nanocavity geometry. *Langmuir* **2021**, *37*, 7008–7018.

[36] Alajmi, A. F.; Alajmi, J.; Adouane, M. Investigation of the physical and chemical properties of dust accumulation and its impact on solar photovoltaic performance in a high-temperature and high-soiling frequency region. *Int. J. Energy Res.* **2026**, *2026*, 5840573.

[37] Yu, Z. L.; Guo, B. K.; Sha, P. W.; Yu, S. N.; Li, P. P.; Xu, Z. Z.; Guo, Y. T.; Xin, R. L.; Chen, L. X.; Gao, D. L. et al. Bionic microstructure/nanofiller heterogeneous ultradurable superhydrophobic surface based on metal additive manufacturing. *Nano Lett.* **2025**, *25*, 7533–7542.

[38] Zhou, X. H.; Ou, J. F.; Hu, Y. T.; Wang, F. J.; Fang, X. Z.; Li, W.; Chini, S. F.; Amirfazli, A. Robust superhydrophobic coating for photothermal anti-icing and de-icing via electrostatic powder spraying. *Prog. Org. Coat.* **2024**, *197*, 108778.

[39] Nomeir, B.; Lakhouil, S.; Boukheir, S.; Ali, M. A.; Naamane, S. Durable and transparent superhydrophobic coating with temperature-controlled multi-scale roughness for self-cleaning and anti-icing applications. *Prog. Org. Coat.* **2024**, *189*, 108338.

[40] Rakheja, T.; Pathak, P.; Grewal, H. S. Facile fabrication of super-slippery and transparent glass with anti-fogging and self-cleaning characteristics. *Mater. Lett.* **2024**, *366*, 136506.

[41] Jin, S. J.; Wang, S. X.; Feng, H. L.; He, H. Y.; Huang, M. J.; Jin, S. L.; Yang, D. R.; Wang, L. Mechanically robust and self-cleaning antireflective coatings for photovoltaic modules. *Sol. Energy Mater. Sol. Cells* **2024**, *275*, 113009.

[42] Zhang, D.; Zhang, J. R.; Zhang, L. Q.; Ji, J. C.; Shen, Y. Q.; Liu, X.; Lu, H. B. Femtosecond laser preparation of superhydrophobic surfaces on PV glass with excellent self-cleaning performance and stability. *Appl. Surf. Sci.* **2026**, *717*, 164765.

[43] Cho, E.; Park, S.; Cho, S.; Lee, S. J. Wide-angle light trapping by irregularly shaped nanostructures for high-performance flexible organic solar cells. *Appl. Surf. Sci.* **2026**, *717*, 164789.

[44] Luo, X. Y.; Sun, W.; Xiong, Z. C.; Chang, Y.; Ren, W. Y.; An, X. Y.; Wang, H.; An, H. C. Hybrid Ag nanocone-Al_2O_3/Si nanopillar periodic array for broadband anti-reflection. *Discover Nano* **2025**, *20*, 144.